



**POLITECNICO**  
MILANO 1863

[RE.PUBLIC@POLIMI](mailto:RE.PUBLIC@POLIMI)

Research Publications at Politecnico di Milano

## Post-Print

This is the accepted version of:

S. Silvestrini, M. Piccinin, G. Zanotti, A. Brandonisio, I. Bloise, L. Feruglio, P. Lunghi, M. Lavagna, M. Varile

*Optical Navigation for Lunar Landing Based on Convolutional Neural Network Crater Detector*

Aerospace Science and Technology, Published online 18/03/2022

doi:10.1016/j.ast.2022.107503

The final publication is available at <https://doi.org/10.1016/j.ast.2022.107503>

Access to the published version may require subscription.

**When citing this work, cite the original published paper.**

© 2022. This manuscript version is made available under the CC-BY-NC-ND 4.0 license  
<http://creativecommons.org/licenses/by-nc-nd/4.0/>

Permanent link to this version

<http://hdl.handle.net/11311/1205476>

# Optical Navigation for Lunar Landing based on Convolutional Neural Network Crater Detector

Stefano Silvestrini<sup>a</sup>, Margherita Piccinin<sup>a</sup>, Giovanni Zanotti<sup>a</sup>, Andrea Brandonisio<sup>a</sup>, Ilaria Bloise<sup>b</sup>, Lorenzo Feruglio<sup>b</sup>, Paolo Lunghi<sup>a</sup>, Michèle Lavagna<sup>a</sup>, Mattia Varile<sup>b</sup>

<sup>a</sup>*Politecnico di Milano – Department of Aerospace Science and Technology, via La Masa, 34, Milano, 20134, MI, Italy*

<sup>b</sup>*AIKO S.R.L., via Dei Mille, 22, Torino, 10123, TO, Italy*

---

## Abstract

Traditional vision-based navigation algorithms are highly affected from non-nominal conditions, which comprise illumination conditions and environmental uncertainties. Thanks to the outstanding generalization capability and flexibility, deep neural networks (and AI algorithms in general) are excellent candidates to solve the aforementioned shortcoming of navigation algorithms. The paper presents a vision-based navigation system using a Convolutional Neural Network to solve the task of pinpoint landing on the Moon using absolute navigation, namely with respect to the Mean Earth/Polar Axis reference frame. The Moon landing scenario consists in the spacecraft descent on the South Pole from a parking orbit to the powered descent phase. The architecture features an Object Detection Convolutional Neural Network (ODN) trained with supervised learning approach. The CNN is used to extract features of the observed craters that are then processed by standard image processing algorithms in order to provide pseudo-measurements that can be used by navigation filter. The craters are matched against a database con-

taining the inertial location of the known craters. An Extended Kalman Filter with time-delayed measurements integration is developed to fuse optical and altimeter information.

*Keywords:* Vision-based navigation, Absolute navigation, CNN Craters detection, Lunar landing

---

## 1. Introduction

Lunar environment and Artificial Intelligence are becoming increasingly attractive to the Space research community, due to the latest long-term plans of Space Agencies. On one hand, the activities linked to the Lunar Gateway have renovated the deep interest in the mentioned environment [1, 2, 3, 4]. On the other hand, recent advancement in research demonstrate the use of Artificial Intelligence for different tasks in the space domain, from navigation [5, 6] to formation flying guidance and control [7, 8, 9]. In this work, the development of a vision-based navigation system using AI to solve the task of pinpoint landing on the Moon is presented. The considered lunar landing scenario is defined by the spacecraft descent on the South Pole, covering the altitude range from 100 km to 3 km. The proposed navigation strategy is subdivided in two main phases which are slightly overlapped for safety reason: one where absolute navigation is performed, the other estimating instead the relative state with respect to the targeted landing site. The current paper focuses on the absolute navigation scenario. The basic idea is to exploit a coupled architecture, between a navigation filter and an AI-assisted Image Processing (AI-IP) system comprised by neural networks and standard image processing algorithms. The AI-IP will be able of processing images

20 acquired by a navigation camera, generating pseudo-measurements that can  
21 be exploited by a sensor-fusion filter, to retrieve the estimated state. In par-  
22 ticular, literature demonstrates that craters database matching is typically  
23 exploited to retrieve the absolute pseudo-measurement [10, 11]. In these  
24 papers, the database matching is performed via nearest neighbor approach,  
25 linking the output from the object detector to the navigation filter.

26 In recent years, the evolution of specialized computing processors, like  
27 Tensor Processing Units (TPU) and Vision Processing Units (VPU), and the  
28 correspondent increment of available computational power paved the way  
29 for future AI-assisted space systems. Some early applications were already  
30 tested in orbit [12, 13]. Guidance, Navigation, and Control, and Vision-  
31 based navigation in particular, could potentially achieve large benefits from  
32 the introduction of such systems.

33 Different solutions were proposed. In [14] a Convolutional Neural Network  
34 (CNN) is coupled with a Long-Short Term Memory (LSTM) to achieve an  
35 end-to-end learning for estimating the 6-DoF pose of a UAV during landing.  
36 The global position and orientation of the robot are the final outputs of the  
37 AI architecture using images and IMU measurements as inputs. A similar  
38 concept structure (CNN+LSTM) is proposed and extended by [15], where the  
39 final output of the AI system is not the pose estimation, but a thrust control  
40 profile to drive the spacecraft in a lunar landing maneuver, mapping the input  
41 of the navigation sensors directly to the control action. A Recurrent CNN  
42 (RCNN) is adopted in [16] to perform end-to-end 6-DoF visual odometry:  
43 the proposed approach exploits a deep learning system based on a monocular  
44 visual odometry (VO) algorithm to estimate poses from raw RGB images.

45 [17] uses a CNN to estimate the depth field of the scene. Information output  
46 by the AI is then passed to an optimization algorithm that filters and refine  
47 the pose estimation. Craters identification has been proposed as a viable  
48 method to perform absolute navigation during lunar landing. State of the  
49 art detectors make use of Object Detection Networks (ODN) [18, 19] image  
50 segmentation [20, 21, 22]. In order to perform end-to-end navigation, craters  
51 detected by the AI requires to be matched with a database. Geometrical [23,  
52 24] or feature-based [25] algorithms were proposed. Finally, object detection  
53 algorithms using Deep Convolutional Networks have been proposed for UAV  
54 obstacle avoidance in [26].

55 The objective of the paper is to present the baseline architecture for such  
56 intelligent vision-based navigation strategy, together with some preliminary  
57 results of the algorithm implementation. In particular, the paper fulfills the  
58 following objectives:

- 59 • the development of a synthetic image generation pipeline to generate  
60 the training dataset and the testing trajectory frames;
- 61 • the creation of a customized CNN to work out the task of crater detec-  
62 tion in Moon images;
- 63 • the derivation of a customized and efficient routine to perform database  
64 filtering and matching to retrieve the absolute location of detected  
65 craters;
- 66 • the development of an Extended Kalman Filter to carry out the navi-  
67 gation estimation based on AI-IP pseudo measurements and altimeter  
68 reading, taking into account the measurements delay.

69 The following sections are structured as follows. In Section 2, the ref-  
70 erence Moon landing scenario is presented, detailing the considered landing  
71 phases. In Section 3, the proposed complete architecture for the absolute  
72 navigation is detailed, from the adopted neural network down to the navi-  
73 gation filter. Simulations results and achieved performance are expounded  
74 in Section 4, while conclusions are drawn in Section 5, with highlights for  
75 planned future steps.

## 76 **2. Moon Landing: Scenario Definition**

77 The considered mission scenario consists in the spacecraft descent from  
78 an altitude of 100 km down to 3 km targeting the Lunar South Pole area, the  
79 designated candidate target for human missions incoming in the next years  
80 [27, 28]. Even if the problem of autonomous guidance generation is out of  
81 the scope of the present study, feasible trajectories are required to test the  
82 proposed AI-based navigation on representative cases. Thus, spacecraft tra-  
83 jectories will be generated executing optimal guidance algorithm depending  
84 on the target location and thrust constraints. Moreover, due to the given  
85 landing location, it is critical to take into account illumination and shad-  
86 owing condition. Since the angle between the Moon rotation axis and the  
87 ecliptic is close to  $90^\circ$ , in the Polar Regions the topography plays a crucial  
88 role in the determination of the illumination conditions. In fact, areas at  
89 relatively high altitude can experience continuous periods of illumination (of  
90 several months), whereas some crater bottoms are always in shadow. In such  
91 scenario, the navigation system can encounter highly varying illumination  
92 conditions, with low Sun elevation angle in the South Pole region and large

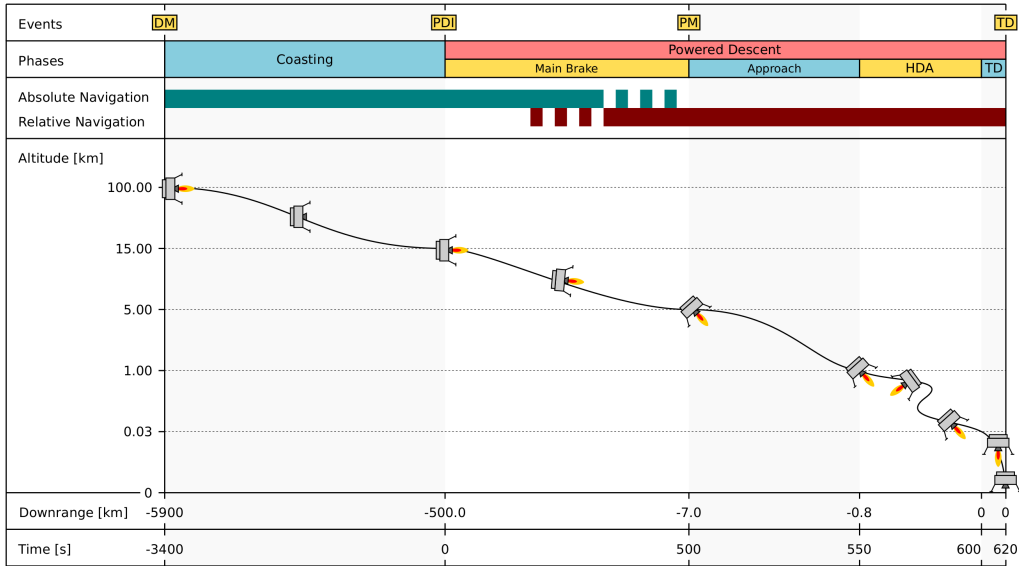


Figure 1: Nominal Lunar Landing Phases and Navigation modes. Distances and times are not in scale. The time scale takes the PDI as origin, while Downrange is assumed to be 0 at the Landing Site.

93 shadow areas in the image. Figure 1 shows the assumed nominal phases for  
 94 a Lunar landing mission. It can be seen how on-board Navigation operates  
 95 in two modes, Absolute and Relative.

96 The spacecraft is assumed to initiate the landing maneuver from a circular  
 97 Parking Orbit (PO) with altitude between 100 and 250 km. The spacecraft  
 98 performs a tangential burn to lower the orbit perilune, inserting itself into an  
 99 elliptical orbit. The lower the perilune, the lower the overall amount of fuel  
 100 required for the landing maneuver. At the same time, the terrain topography  
 101 poses a safety requirement on the minimum altitude of the perilune. 15 km is  
 102 a generally accepted value and is adopted as nominal value in this study. At  
 103 the perilune of the transfer orbit the Powered Descent Initiation takes place:

104 the main thrusters are turned on and the spacecraft performs the Main Brake  
105 maneuver, in which most of the horizontal is dropped. The thrust magnitude  
106 is constant and close to the maximum. The thrust vector pointing profile  
107 is optimized and remains close to the local horizon. During most of this  
108 phase the navigation is absolute, while in the last part relative navigation is  
109 initialized, for it is required to be already active and running at the beginning  
110 of the next phase. As the nominal landing site comes into the field of view  
111 of the navigation system, the Final Approach phase begins. The constant  
112 thrust constraint is released and the S/C performs a pitch maneuver to point  
113 the thrust vector mainly toward ground. In this phase relative navigation is  
114 performed; the landing area is scanned and large diversions to the landing  
115 trajectory can be commanded to cope with errors. Below 1500 m of altitude,  
116 fine trajectory corrections (in the maximum order of magnitude of hundreds  
117 of meters) can be ordered to perform the Hazard Avoidance task. This phase  
118 ends on the vertical of the selected landing site at a certain altitude (tens  
119 of meters), with null horizontal velocity. Pinpoint landing terminates with a  
120 powered vertical descent at constant velocity until the touchdown. Absolute  
121 navigation, which constitutes the main focus of this work, is operative from  
122 the parking orbit until the beginning of the Approach phase.

123 To ease the formulation of the reference landing maneuver, without loss  
124 of generality, in this work is assumed that the inclination of the initial PO  
125 can be tuned to match the latitude of the target landing site achieving a  
126 planar trajectory (in the inertial reference frame). Nevertheless, the planar  
127 assumption is not valid in a Lunar Fixed Frame (LFF), due to the Moon  
128 rotation. Such reference frame corresponds to the Mean Earth/Polar Axis



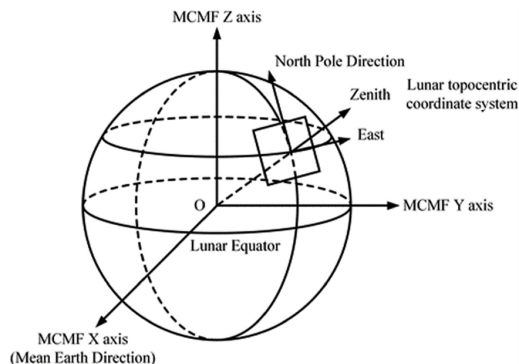


Figure 2: Lunar Fixed Frame Mean Earth/Polar Axis. Figure from [29] by GUO et al.

129 (ME), as shown in Fig. 2, described in details in [29]. It defines the z-axis as  
 130 the mean rotational pole, while the Prime Meridian ( $0^\circ$  Longitude) is defined  
 131 by the mean Earth direction. The intersection of the lunar Equator and  
 132 Prime Meridian occurs at what can be called the Moon’s “mean sub-Earth  
 133 point”, due to the Moon’s tidal locking to the Earth. In absolute navigation,  
 134 the state of the spacecraft is reconstructed with respect to the LFF. The effect  
 135 of the Moon’s rotation corresponds to a maximum velocity in the Crossrange  
 136 direction approximately equal to  $4.5 \text{ m s}^{-1}$  during the coasting phase. In the  
 137 models, simulations, and generation of the image dataset used to train, test,  
 138 and verify the AI system, this effect shall be taken into account.

139 The times of the transitions between the Main Brake and the Approach,  
 140 and between the Approach and the Hazard Avoidance, come out from a  
 141 complex optimization performed in the mission design phase, and depend on  
 142 the combination of several parameters, related to the controllability of the  
 143 lander (thrust and torque maximum magnitude, divert capabilities), and to  
 144 the constraints imposed by hazard detection and navigation capabilities.

145 *2.1. Reference landing maneuver*

146 Figure 3 reports the specific application case used as reference in this  
147 work. The lander mass at PDI is assumed to be 1500 kg. The available  
148 thrust during the Main Brake is assumed to be 3800 N, while during the Fi-  
149 nal Approach and in the subsequent phases it is considered to be throttleable  
150 between 1000 and 2300 N. The main engine is assumed to be tightly con-  
151 nected to the S/C structure with no thrust vector control, linking the thrust  
152 pointing direction directly with the S/C attitude. Trajectory has been opti-  
153 mised to minimize the fuel consumption; a direct optimization method has  
154 been used for the main brake phase, combined with the semi-analytical DA  
155 guidance described in [30] for the Final Approach. The optimization does  
156 not include the coasting phase, which is purely ballistic and in first approx-  
157 imation can be assumed to be a perfect Keplerian arc of an elliptical orbit.  
158 Figure 3a shows the nominal altitude profile, starting at the PDI. It can  
159 be seen how at the beginning the high tangential speed tends to follow the  
160 transfer orbit trajectory and the altitude increases. Then, as the drop in the  
161 horizontal velocity becomes relevant, the altitude begins to decrease. Fig-  
162 ures 3b and 3c show respectively the horizontal and vertical velocity profiles:  
163 most of the horizontal velocity is dropped in the Main Brake, with a velocity  
164 in the order of magnitude of  $100 \text{ m s}^{-1}$  at the beginning of the Approach.  
165 The profile of the thrust angle (corresponding to the pitch angle) is shown  
166 in Fig. 3d. It is considered to be 0 whenever pointing toward the horizon,  
167 and  $-90^\circ$  with the thrust vector pointing downward (vertical attitude). The  
168 pitch maneuver at the end of the main brake, corresponding to an altitude  
169 of  $\sim 4000 \text{ m}$  is clearly visible. Finally, Fig. 3f reports the view angle on the

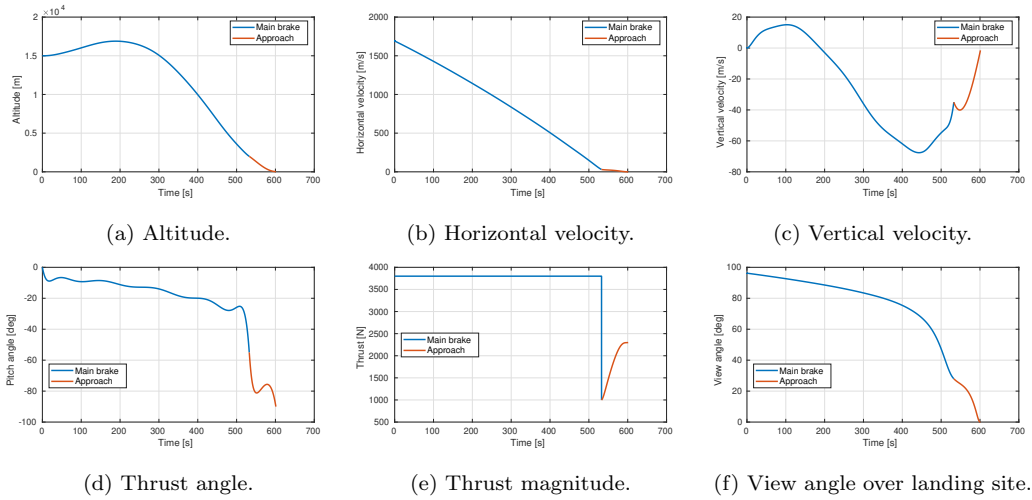


Figure 3: Nominal landing maneuver (powered descent and final approach only).

170 nominal landing site from the lander, an information of particular relevance  
 171 in a relative navigation scenario, not covered in this work. No specific epoch  
 172 is assumed for the initiation of the maneuver, nor RAAN for the parking  
 173 orbit. In this way, the reference maneuver can be adapted to different initial  
 174 conditions, exposing the navigation system to completely different portions of  
 175 lunar terrain, giving the possibility to test the system in different conditions.

## 176 2.2. Camera and illumination conditions assumptions

177 A camera with  $40^\circ$  Field Of View (FOV) and a  $1024 \times 1024$  pixels sensor  
 178 is assumed as main navigation sensor. During the powered descent the trans-  
 179 lation of the S/C is controlled in open-loop mode, with the lander tracking a  
 180 profile of attitude and thrust magnitude computed by the on-board guidance  
 181 module. In order to cope with error propagation, the trajectory is periodi-  
 182 cally recalculated, converging progressively to the target. An estimation of  
 183 the lander state in terms of position and velocity relative to the target is

184 then required only for periodically trajectory update. From past studies, it  
185 is known that such system can be effective with a minimum frequency of  
186 the trajectory update of 0.2 Hz [30, 31]. Beyond certain frequencies the gain  
187 in performance due to the faster update becomes irrelevant. Taking some  
188 margin, a minimum requested frequency of 1 Hz is assumed for the image  
189 feeding to the navigation.

190 During the coasting phase, the S/C travels half of the transfer orbit,  
191 covering 180 degrees in true anomaly. That implies that the illumination  
192 conditions on ground, especially the inclination of the Sun over the terrain,  
193 that the navigation system is expected to encounter are extremely variable,  
194 from the Sun slightly above the horizon in polar regions to 90° of Sun elevation  
195 close to the Lunar Equator. No particular constraints that bounds the Sun  
196 inclination to a specific range is assumed.

### 197 **3. Absolute Navigation Architecture**

198 The absolute navigation task requires the determination of the complete  
199 state, i.e. position and velocity with respect to the inertial system fixed to  
200 the Moon. The optical measurements are fed to a convolutional neural net-  
201 work, which is trained to identify the database craters present in the image.  
202 Such correspondence is later fed to a navigation filter that performs sensor  
203 fusion with an altimeter present on-board. A schematic of the architecture  
204 is reported in Fig. 4.

#### 205 *3.1. Crater database and AI training set generation*

206 The task of absolute navigation is to estimate the lander position and  
207 velocity with respect to the LFF. Thus, the ultimate goal is to retrieve such

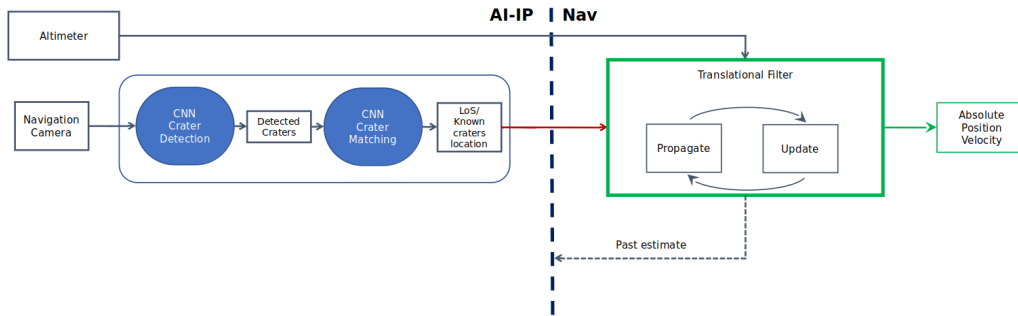


Figure 4: Schematic of absolute navigation modules.

208 information from the craters identified in the image.

### 209 3.1.1. Dataset elements

210 The objective of the AI algorithm is to detect craters on the lunar surface.  
 211 For training purposes, a dataset has been created, formed by the following  
 212 fundamental elements:

- 213 • a set of images of the lunar terrain;
- 214 • the list of the visible craters in each image, with centers positions and  
 215 radii in camera coordinates;
- 216 • for each image, the correspondent absolute position and attitude of the  
 217 lander relative to LFF;
- 218 • a crater database including the position (or alternatively the latitude/longitude  
 219 pair) of each labeled crater in the LFF.

### 220 3.1.2. Dataset generation framework

221 An artificial Digital Elevation Model (DEM) of the Moon has been ex-  
 222 ploited to generate simulated images taken by a landing navigation camera,

223 to create both the AI training dataset and end-to-end simulations of com-  
224 plete landing maneuvers used to evaluate the overall system performances in  
225 Section 4. The simulated portion of the Moon used for generating the dataset  
226 is a DEM modeled in Pangu, an high fidelity rendering software meant for  
227 space applications and realistic rendering of natural celestial bodies [32]. A  
228 flat DEM is created, perturbed with fractal noise and enriched with the other  
229 relevant terrain features, i.e. craters. A detailed crater database is needed  
230 to perform lunar absolute navigation with the proposed architecture. This  
231 method allows to have a completely reliable ground-truth for the craters po-  
232 sition and size, while real DEMs present craters that are not registered in  
233 databases and would not allow to build a completely reliable training set.

234 In order to generate a rich and representative dataset, the environmental  
235 variables in Table 1 are randomly varied within the reported ranges. By  
236 doing so, the dataset can cover the wide feature-space that is expected in the  
237 operational scenario. The lunar impact crater size and distribution has been  
238 extracted from [33].

239 The craters reported in Table 1 refer to the synthetic generation per-  
240 formed in Pangu. In the ballistic trajectory during the coasting phase, the  
241 S/C travels half of the transfer orbit, covering  $180^\circ$  in true anomaly. That  
242 implies that the illumination conditions on ground, especially the inclination  
243 of the Sun over the terrain, that the navigation system is expected to en-  
244 counter are extremely variable, from the Sun slightly above the horizon in  
245 polar regions to potentially straight illumination with  $90^\circ$  of Sun elevation  
246 close to the Lunar Equator. Regarding the Sun Azimuth angle, considering  
247 the South Pole region, it is related to the Moon rotation. Therefore, it can

Table 1: Environmental variables and their range of variation for the dataset generation.

Variable	Range
Altitude	3 - 100 km
Attitude pitch (wrt vertical)	0° - 20°
Sun illumination angle - Elevation	0° - 90°
Sun illumination angle - Azimuth	0° - 360°
Synthetic crater frequency	1.8e6 - 3e6
Synthetic craters dimension	6 - 500 m

248 vary in the whole range between 0° to 360°. Actually, this wide range is ap-  
 249 plicable only for high latitudes close to the Poles. No particular constraints  
 250 that bound the Sun inclination to a specific range (like the execution of the  
 251 whole landing maneuver close to the lunar terminator) are assumed.

252 For the dataset, 5000 images have been generated: some examples of  
 253 images stored in the dataset are reported in Fig. 5a, with the ground-truth  
 254 craters present in the images highlighted in Fig. 5b.

### 255 3.2. Neural network training set

256 In order to perform the training of the neural network, the dataset de-  
 257 scribed in Section 3.1.2 is completed with the information related to the  
 258 craters actually visible in each frame. Each image is associated with the list  
 259 of the craters comprised in the current field of view; the coordinates of each  
 260 crater are converted into a bounding box, expressed by a vector of coordi-  
 261 nates in the image reference frame  $[y_{\min}, x_{\min}, y_{\max}, x_{\max}]$ . The pairs (image,  
 262 list of bounding boxes) constitute the actual training set for the subsequent

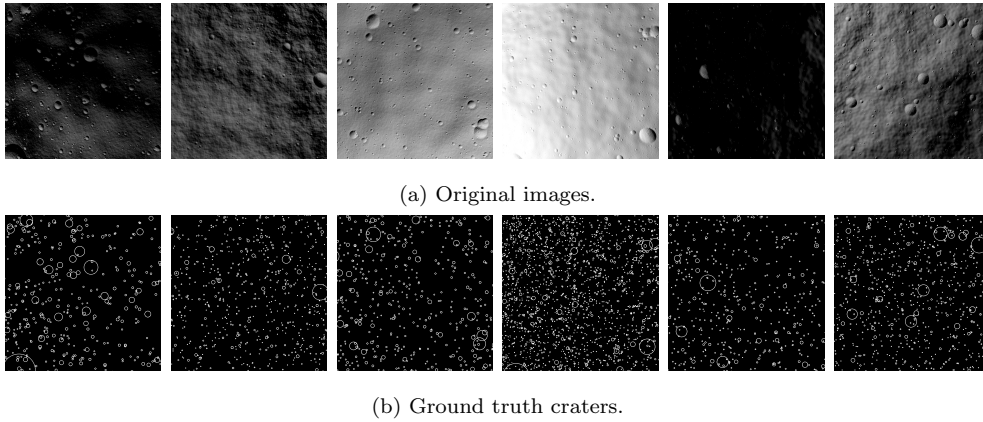


Figure 5: Training set examples.

263 neural network: the image is the network input, while the list of bounding  
 264 boxes constitutes the network target.

### 265 3.3. CNN for crater detection

266 Convolutional Neural Networks are particularly suited for replacing effec-  
 267 tively some of the traditional image processing algorithms. Several, different  
 268 network structures can be conceived basing on CNNs. State of the art crater  
 269 detection networks rely heavily on the so called U-Net architecture [34, 35]  
 270 to identify landmarks by means of image segmentation [20, 21, 22]. For the  
 271 first half of its layers, the network downsamples, and then upsamples for  
 272 the second half, while maintaining short-cut connections between the lay-  
 273 ers. Finally, it uses template matching to extract the craters from the target  
 274 masks. Despite its high accuracy, such architecture involves a huge number  
 275 of trainable parameters, with a computational cost accordingly high. Pre-  
 276 liminary tests performed with such architecture confirmed this trend, with a  
 277 computational burden potentially too high to achieve the target of at least



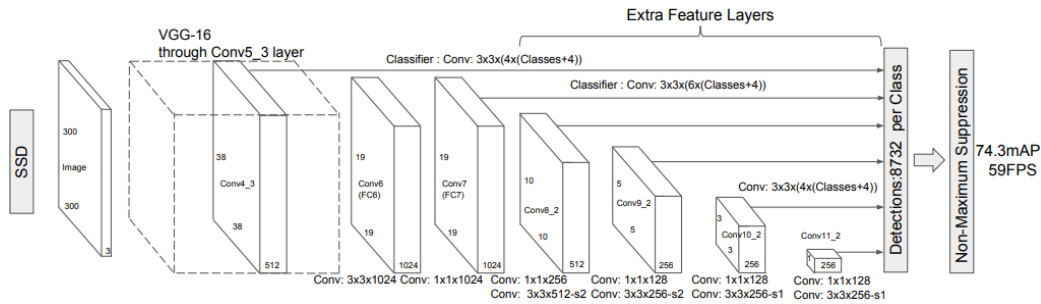


Figure 6: Single Shot Detection (SDD) network from [36] by Liu et al. The original feature extractor is based on VGG-16; a fully convolutional network is then used to estimate both the class and the bounding box associated to each object in the image.

278 one image processed per second on flight-representative hardware.

279 To reduce both the computational cost and the training time, a state-  
 280 of-art Object Detector Network (ODN) is considered. Pre-trained models  
 281 are already available in Tensorflow Object Detection API framework. The  
 282 collection has models trained on benchmark datasets such as COCO, KITTI  
 283 and Open Images: such models are available for initialization of new custom  
 284 models and to train them on novel datasets. The structure of the network  
 285 used in the implementation is based on a Single Shot Detector (SDD) [36]  
 286 with MobileNetV2 [37], pre-trained on the COCO dataset [38], as feature ex-  
 287 tractor. SDD combined with MobileNetV2 ensures computational efficiency  
 288 and fast inferences on the embedded system thanks to the use of optimized  
 289 operations like depth-wise separable convolutions [39] instead of basic con-  
 290 volutions.

291 The basic structure of a SDD network is shown in Fig. 6: in this work,  
 292 with respect to the original version represented in the graph, the VGG-16  
 293 feature extractor has been replaced with the more computationally efficient

294 MobileNetV2. Transfer learning allows to exploit the efficient set of low level  
295 features that pre-trained networks offer: nevertheless, the specific, selected  
296 network imposes some constraints on the size of the input frame, that has  
297 to fit the pre-trained architecture. An additional preprocessing step is then  
298 requested: first, the image is scaled down to the  $320 \times 320$  px resolution,  
299 then is converted back in a 3-channel image, achieving a final frame size  
300 equal to  $320 \times 320 \times 3$ , which is the original input size of the MobileNetV2.  
301 The conversion from single channel to RGB comes with null computational  
302 cost, for the information of the original channel is just replicated 3 times.  
303 The downscaling is selected for mainly two reasons: on one hand, in this  
304 way, the size of the input is kept unaltered to meet the original input of  
305 the MobileNetV2; on the other hand, increasing the input size affects the  
306 inference time, which is potentially crucial for the next implementation of  
307 the algorithm into real hardware.

308 The output consists in a  $n \times 5$  matrix reporting the list of the craters  
309 located in the image. Each row, corresponding to a single detection, is a  
310 5-element vector  $[y_{\min}, x_{\min}, y_{\max}, x_{\max}, \alpha]$ , where the first four elements con-  
311 sist in the coordinates of the bounding box enclosing the crater. The origin  
312 of the reference system is conventionally placed in the upper left corner of  
313 the image; values are normalized by image width and height to constrain the  
314 interval between zero and one. The index  $\alpha \in [0, 1]$  is a score representing  
315 the network confidence in the crater identification: low score means little  
316 confidence in saying that the output coordinates correspond to the bounding  
317 box of a crater. Only craters detected with high confidence  $\alpha \geq \bar{\alpha}$  are con-  
318 sidered for the subsequent navigation step. The threshold  $\bar{\alpha}$  is an adjustable

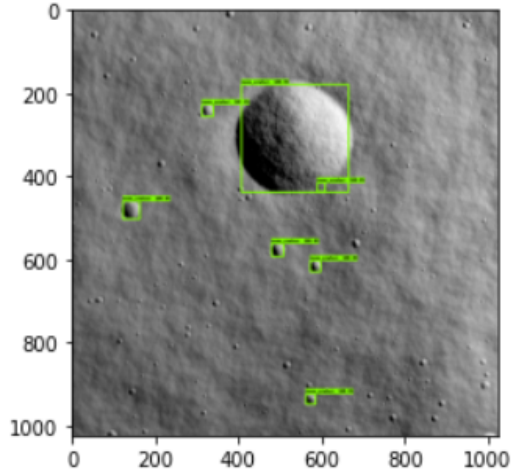


Figure 7: Output of the ODN. Bounding boxes around detected craters.

319 hyperparameter of the navigation system: in the remainder of the paper,  
 320  $\bar{\alpha} = 0.6$  is assumed. Standard ODNs are trained to recognize multiple types  
 321 of objects, and each bounding box has an associated class; in this particular  
 322 case, the network is trained to detect a single "crater" class. An example of  
 323 the network output is shown in Fig. 7.

324 Post-processing is performed on the network output to retrieve the craters  
 325 coordinates given the bounding boxes predicted by the AI model. The step-  
 326 wise procedure is summarized here:

- 327 • Selection of the predicted bounding boxes according to the confidence  
 328 threshold  $\bar{\alpha}$  and Intersection-Over-Union threshold,  $\text{IoU} \geq \overline{\text{IoU}}$  (set to  
 329 0.1). Intersection-Over-Union is used in non max suppression, which is  
 330 used to eliminate multiple boxes that surround the same object, based  
 331 on which box has a higher confidence. The building blocks of this  
 332 process are:

- 333           – Compare the most confident bounding box with its IoU with every
- 334           other predicted bounding box of the crater class. If the  $\text{IoU} \geq \overline{\text{IoU}}$ ,
- 335           discard it as it represents a duplicate detection.
- 336           – Remove the output predicted bounding box from the list of bound-
- 337           ing boxes.
- 338       • Calculate the center and diameter to inscribe each rectangular bound-
- 339       ing box into a circle.

340 In this way, bounding box coordinates are converted in a 3-element vector  
 341  $[x, y, \rho]$ , where  $x$  and  $y$  are the coordinates of the crater’s center, and  $\rho$   
 342 its radius, directly comparable with the craters database. An example is  
 343 shown in Fig. 8. One of the major concerns with CNN and AI in general  
 344 is their generalization ability, and the proper behavior of the model when  
 345 performing inferences on real data is not assured when the training is based  
 346 on synthetic data. Although this aspect needs to be tackled at a systematic  
 347 level, which is beyond of the scope of this paper, the trained ODN detector  
 348 has been qualitatively assessed with real Moon images. The results are shown  
 349 in Fig. 9.

#### 350 *3.4. Database Filtering and Matching*

351       The first task of the navigation module consists in matching the detected  
 352 craters  $c_{odn}$ , expressed in image frame coordinates, to real database craters.  
 353 In this way, the absolute location of identified features, i.e. craters, can be  
 354 retrieved. The task requires the feedback knowledge coming from the nav-  
 355 igation estimate of the spacecraft position vector. The FOV of the camera

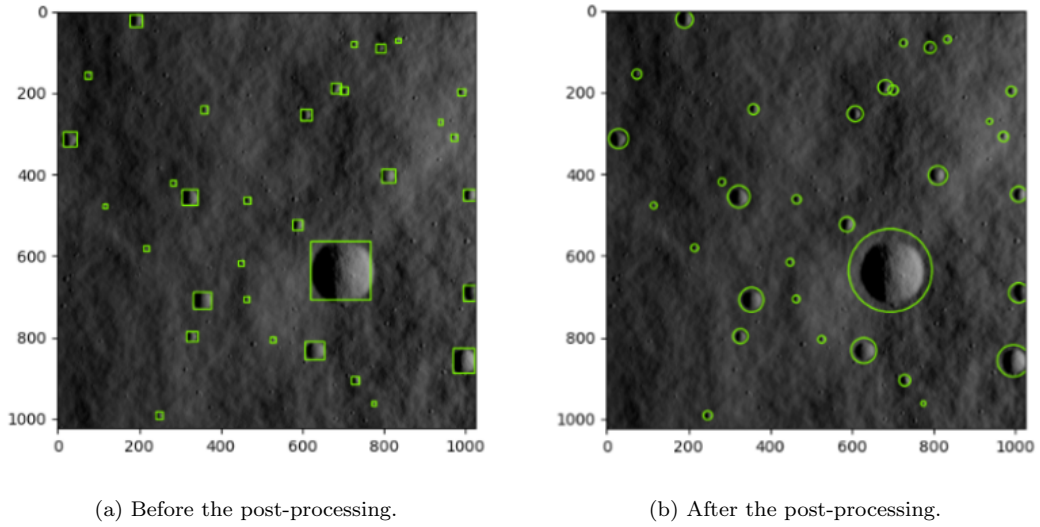


Figure 8: ODN post-processing. Bounding boxes are converted into craters' positions and radii.

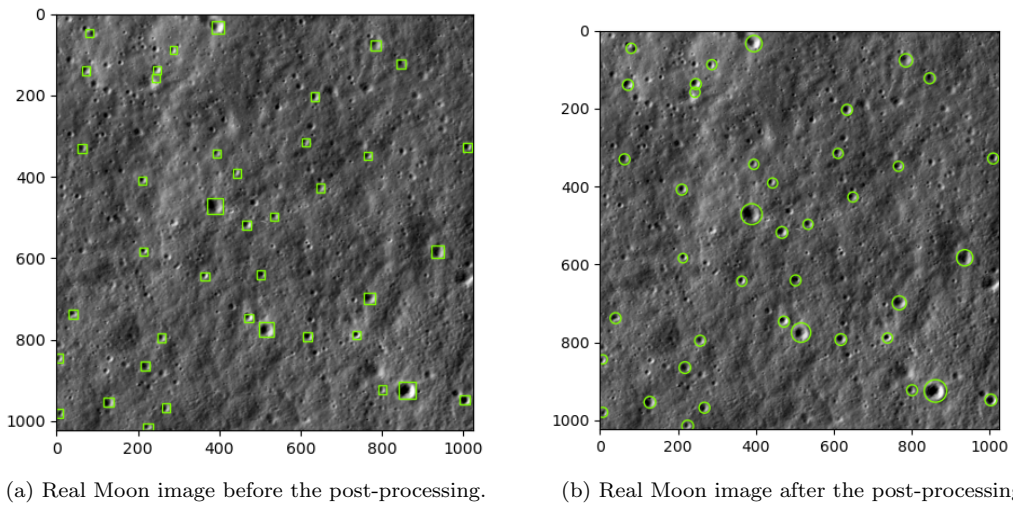


Figure 9: Real Moon image ODN post-processing. Bounding boxes are converted into craters' positions and radii. Moon image taken from LROC database [40].

356 is projected on the surface using spherical projection. In other words, find-  
 357 ing the intersection between a sphere and a line one needs to combine the  
 358 equations:

$$\|\mathbf{x} - \mathbf{c}\|^2 = r^2 \quad (1)$$

359 where  $\mathbf{x}$  are the points on the sphere,  $\mathbf{c}$  the center point and  $r$  radius of the  
 360 sphere.

$$\mathbf{y} = \mathbf{o} + d\hat{\mathbf{u}} \quad (2)$$

361 where  $\mathbf{y}$  are points on the line,  $\mathbf{o}$  the origin of the line and  $d$  the distance  
 362 from the origin along the line and  $\hat{\mathbf{u}}$  the direction of line (a unit vector). The  
 363 origin is the focal point of the ideal camera.

364 The output of the projection is a set of corners  $\kappa$ , representing the bound-  
 365 aries of the projected FOV. Each corner is expressed in *latitude* ( $\phi$ ) and *lon-*  
 366 *gitude* ( $\lambda$ ) coordinates. The margined search area  $\mathcal{A}$  is a spherical region  
 367 constructed by extracting the maximum *lat-lon* coordinates out of the  $\kappa$  cor-  
 368 ners, as shown in Fig. 10. The extracted database craters  $c_{db}$  coordinates are  
 369 first expressed in the inertial frame, then they are projected into the camera  
 370 frame.

$$\forall c_{db} \in \mathcal{A}, (\lambda, \phi) \rightarrow (X, Y, Z)_I \rightarrow (l_x, l_y, l_z)_C = A_{C/I}(X, Y, Z)_I \quad (3)$$

371 Finally, the homographic projection is used to retrieve the 2D coordinates  
 372 of each crater in the image frame, as reported in Eq. 8. At this point, the  
 373 algorithm possess two lists of craters expressed in the image frame:  $c_{db}$  is the  
 374 query grid out of which the craters in the list  $c_{odn}$  are matched.

375 The matching task is performed using a traditional 1-nearest neighbor  
 376 routine, the list of craters are organized into a KD-tree to facilitate the

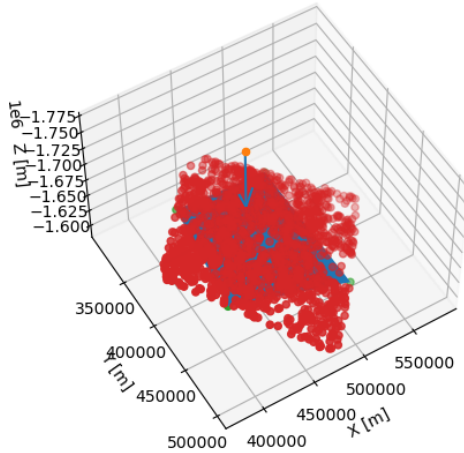


Figure 10: Margined search area  $\mathcal{A}$  containing the projected FOV.

377 matching procedure. The features used for matching are obviously the craters  
 378 location coupled with the projected diameter. The craters database matching  
 379 outputs a set of inertial coordinates of craters that have been identified as  
 380 the groundtruth of the ODN detected craters.

### 381 3.5. Absolute Navigation Filter

382 The absolute navigation task is performed by a discrete-time Extended  
 383 Kalman Filter, whose output is the estimate of the complete state  $\mathbf{X}$ , compo-  
 384 sition of position  $\hat{\mathbf{R}}$  and velocity  $\hat{\mathbf{V}}$  vectors. The inputs received are instead  
 385 the AI-IP block products and the output of the altimeter, the former sampled  
 386 at a 1 Hz rate, while the latter at 8 Hz.

387 The dynamics implemented on the filter, used to retrieve the a-priori  
 388 estimate of the state, is given by a simplified two-body dynamics expressed  
 389 in the LFF reference frame with the control component  $\mathbf{U}$ . Eq. 4 reports

390 the complete expression of the right-hand-side of the implemented dynamics  
391  $\mathbf{f}(\mathbf{X})$ , where  $GM_{\mathcal{C}}$  is the gravitational parameter of the Moon and  $\boldsymbol{\Omega} =$   
392  $[0, 0, \Omega]^\top$  is the angular velocity of the Moon rotation about its own axis,  
393 expressed in the LFF, which coincides with the angular velocity of the non-  
394 inertial reference frame.

$$\dot{\mathbf{X}} = \mathbf{f}(\mathbf{X}) = \begin{bmatrix} \dot{R} \\ \dot{V} \end{bmatrix} = \begin{bmatrix} \dot{V} \\ -\frac{GM_{\mathcal{C}}}{\|\mathbf{R}\|^3} \mathbf{R} + \mathbf{V} \wedge \boldsymbol{\Omega} + \boldsymbol{\Omega} \wedge \mathbf{R} \wedge \boldsymbol{\Omega} + \mathbf{U} \end{bmatrix} \quad (4)$$

The Jacobian matrix deriving from such expression is instead given by Eq. 5.

$$\mathbf{F} = \begin{bmatrix} \mathbf{0}_{3 \times 3} & \mathbf{I}_{3 \times 3} \\ \mathbf{F}_{VR} & \mathbf{F}_{VV} \end{bmatrix} \quad (5)$$

$$\text{with } \mathbf{F}_{VR} = \frac{GM_{\mathcal{C}}}{\|\mathbf{R}\|^3} \begin{bmatrix} 3/\|\mathbf{R}\|^2 X^2 - 1 & 3/\|\mathbf{R}\|^2 XY & 3/\|\mathbf{R}\|^2 XZ \\ & 3/\|\mathbf{R}\|^2 Y^2 - 1 & 3/\|\mathbf{R}\|^2 YZ \\ \text{Sym.} & & 3/\|\mathbf{R}\|^2 Z^2 - 1+ \end{bmatrix} \quad (6)$$

$$+ \begin{bmatrix} \Omega^2 & 0 & 0 \\ 0 & \Omega^2 & 0 \\ 0 & 0 & 0 \end{bmatrix}$$

$$\text{and } \mathbf{F}_{VV} = \begin{bmatrix} 0 & 2\Omega & 0 \\ -2\Omega & 0 & 0 \\ 0 & 0 & 0 \end{bmatrix} \quad (7)$$

395 Concerning instead the measurement models employed, the filter receives  
396 from the AI-IP block both the absolute location  $\rho_i$  and relative line-of-sight  
397  $\mathbf{u}_i$  associated to the  $i^{\text{th}}$  matched crater. The former is expressed in the LFF  
398 frame (see Fig. 2), while the latter is expressed as the two homographic



399 coordinates, projection of the LoS vector onto the on-board camera plane.  
 400 The measurement function that is implemented on the filter is represented  
 401 in Eq. 8.

$$\mathbf{u}_i = \begin{bmatrix} u_{i,x} \\ u_{i,y} \end{bmatrix} = f/l_{i,z} \begin{bmatrix} l_{i,x} \\ l_{i,y} \end{bmatrix} \quad (8)$$

$$\text{with } \mathbf{l}_i = \mathbf{A}_{C/I} \frac{\hat{\mathbf{R}} - \rho_i}{\|\hat{\mathbf{R}} - \rho_i\|} \quad (9)$$

402 Here some parameters have been introduced, namely the focal length  $f$ ,  
 403 the LoS vector in the camera frame  $\mathbf{l}_i$  and the rotation matrix  $\mathbf{A}_{C/I}$  from the  
 404 LFF frame ( $I$ ) to the camera frame ( $C$ ). Given the necessity of retrieving  
 405 the absolute attitude of the spacecraft, a rotational filter is required to be  
 406 running in synchronous advance with respect to the translational filter.

407 These pieces of information are fused together with measurements of the  
 408 satellite altitude  $\zeta$ , taken by an altimeter. As such, the measurement model  
 409 reported in Eq. 10, where  $R_{\mathcal{C}}$  is the average Moon radius.

$$\zeta(\mathbf{R}) = \|\mathbf{R}\| - R_{\mathcal{C}} \quad (10)$$

410 The complete measurement function is then constructed as the collection  
 411 of all the homographic coordinates associated to the detected craters as per  
 412 Eq. (8) with the addition of the altimeter measure estimate, as in Eq. (10).  
 413 The resulting measurement estimate vector  $\mathbf{h}$  is composed by  $2N_{crat} + 1$   
 414 elements, where  $N_{crat}$  is the number of detected craters. The associated  
 415 Jacobian matrix  $\mathbf{H}$  will have a size of  $(2N_{crat} + 1 \times 6)$  and is to be assembled  
 416 with  $N_{crat}$   $(2 \times 6)$   $\mathbf{H}_{i,crat}$  matrices for each crater LoS and with a single

417  $(1 \times 6)$   $\mathbf{H}_{alt}$  for the altimeter part. The complete expressions are omitted  
 418 due to their cumbersome representations.

419 Algorithm 1 reports the most relevant steps of the EKF procedure in a  
 pseudo-code format.

---

**Algorithm 1** Extended Kalman Filter

---

- 1:  $\hat{\mathbf{X}}_k^- = \int_{t_{k-1}}^{t_k} f(\mathbf{X}(\tau))d\tau$ ,  $\mathbf{X}_{k-1} = \hat{\mathbf{X}}_{k-1}$ ,  $\hat{\mathbf{X}}_0^+ = \mathbf{X}_0$  ▷ Absolute state propagation
  - 2:  $\mathbf{F}_k = \left. \frac{\partial f}{\partial \mathbf{X}} \right|_{\hat{\mathbf{X}}_{k-1}}$ ,  $\mathbf{H}_k = \left. \frac{\partial h}{\partial \mathbf{X}} \right|_{\hat{\mathbf{X}}_k^-}$  ▷ State and measurement Jacobian matrices
  - 3:  $\Phi(t_k, t_{k-1}) = \mathbf{I}_{6 \times 6} + \mathbf{F}_k \Delta t$  ▷ State Transition Matrix
  - 4:  $\mathbf{P}_k^- = \Phi(t_k, t_{k-1})\mathbf{P}_{k-1}^+\Phi^T(t_k, t_{k-1}) + \mathbf{Q}$ ,  $\mathbf{P}_0^+ = \mathbf{P}_0$  ▷ State Covariance matrix propagation
  - 5:  $\mathbf{K}_k = \mathbf{P}_k^- \mathbf{H}_k^T (\mathbf{H}_k \mathbf{P}_k^- \mathbf{H}_k^T + \mathbf{R}_k)^{-1}$  ▷ Kalman gain matrix computation
  - 6:  $\hat{\mathbf{X}}_k^+ = \hat{\mathbf{X}}_k^- + \mathbf{K}_k (\mathbf{Y}_k - h(\mathbf{X}_k^-))$  ▷ Absolute State correction
  - 7:  $\mathbf{P}_k^+ = (\mathbf{I} - \mathbf{K}_k \mathbf{H}_k) \mathbf{P}_k^- (\mathbf{I} - \mathbf{K}_k \mathbf{H}_k)^T + \mathbf{K}_k \mathbf{R}_k \mathbf{K}_k^T$  ▷ State Covariance matrix correction
- 

420  
 421 The output of the filter is then fed back in the IP block. The estimate  
 422 of the state can be exploited in order to restrain the research space for the  
 423 pattern matching algorithms. However this additional information for the IP  
 424 block could not be exploited in non-nominal conditions, such as a *lost-in space*  
 425 scenario, reason for which performance assessment without this improvement  
 426 shall be performed as well.

427 *3.6. Time-Delayed Measurements Fusion*

428 The navigation algorithm heavily relies on optical measurements. The  
 429 information content is extracted from the images through the ODN and the  
 430 intermediate post-processing. Such process takes a finite amount of time  
 431 that needs to be taken into account when fusing the measurements in the  
 432 Extended Kalman Filter, especially for real-time applications. Indeed, when  
 433 delayed measurements are presents, at instant  $k$  the system receives a delayed  
 434 measurement corresponding to time instant  $s$  ( $s = k - N$ , where  $N$  number

435 of delay samples). In this paper, a known delay of 1 s is reached in light of  
436 the future hardware implementation. There are various methods to consider  
437 the measurements delays in the navigation filter:

- 438 • Filter recalculation method: it consists of coupling two filters running  
439 at fast and slow rate [41]. The former incorporates the high-frequency  
440 measurements, whereas the latter is activated every time a delayed (e.g.  
441 slow and less frequent) measurement arrives. The method computes the  
442 entire trajectory of the state until the current step. Using this method,  
443 optimality is guaranteed at the cost of computational burden.
- 444 • Alexander Method: it consists on updating the covariance matrices at  
445 time  $s$  as if the delayed measurement arrived. Then, once measure-  
446 ments  $\mathbf{Y}_s$  are inserted at time  $k$ , the update is simply the standard  
447 Kalman Filter one with a correction matrix term [42].
- 448 • Larsen Extrapolation Method: The method described in [42] requires  
449 the measurement matrix  $\mathbf{H}_s$  and the noise distribution matrix  $\mathbf{R}_s$  at  
450 time  $s$ . In the presented scenario, this is not valid: indeed, the mea-  
451 surement matrix depends on the relative positioning of the camera and  
452 craters. Larsen developed a measurement extrapolation method that  
453 does not require knowledge about the two matrices until time  $k$  [43].  
454 Such method is taken as reference to implement a modified version  
455 suitable for the analyzed scenario.

456 The adaptation of the Larsen method for the measurement fusion is hereby  
457 described. For details on the derivation, the reader is suggested to refer to  
458 the original reference [43]. Several modifications were needed to solve two

459 shortcomings of the original method: the incorporation of high-frequency  
460 altimeter and the extension to the nonlinear Extended Kalman Filter. For  
461 the former, the filter firstly computes the gain and the updates as in Algo-  
462 rithm 1 fusing fast altimeter measurements. For what concerns the delayed  
463 measurements, let us call the measurements coming from the time instant  
464  $s = k - N$  as  $\mathbf{Y}_s$ , which are incorporated at time instant  $k$ . The Larsen  
465 method consists in calculating an extrapolated measurements from  $\mathbf{Y}_s$  to be  
466 integrated at time  $k$ , called  $\mathbf{Y}_{k,s}^{ext}$ .

$$\mathbf{Y}_{k,s}^{ext} = \mathbf{Y}_s + h(\hat{\mathbf{X}}_k^-) - h(\hat{\mathbf{X}}_s^+) \quad (11)$$

467 At each intermediate step between  $s$  and  $k$  a correction term  $M$  is calculated  
468 as:

$$\mathbf{M}_k = \left[ \prod_{i=0}^{k-s-1} (\mathbf{I} - \mathbf{K}_{k-i} \mathbf{H}_{k-i}) \Phi(t_{k-i}, t_{k-i-1}) \right] \mathbf{P}_s \quad (12)$$

where the Kalman gain and measurement sensitivity matrix  $\mathbf{H}_{k-i}$  at step  
 $k - i$  does not reflect any update coming from the delayed measurement  $\mathbf{Y}_s$ .  
Then, the updates of the correction term are calculated as follows, modifying  
the correction equations in Algorithm 1:

$$\mathbf{K}_{k,s} = \mathbf{M}_k \mathbf{H}_{k,s}^T [\mathbf{H}_{k,s} \mathbf{P}_s \mathbf{H}_{k,s}^T + \mathbf{R}_s]^{-1} \quad (13)$$

$$\hat{\mathbf{X}}_k^+ = \hat{\mathbf{X}}_k^- + \mathbf{K}_{k,s} (\mathbf{Y}_{k,s}^{ext} - h(\hat{\mathbf{X}}_k^-)) \quad (14)$$

$$\mathbf{P}_k^+ = (\mathbf{I} - \mathbf{K}_{k,s} \mathbf{H}_{k,s} \mathbf{M}_k^T \mathbf{P}_k^{-1}) \mathbf{P}_k^- (\mathbf{I} - \mathbf{K}_{k,s} \mathbf{H}_{k,s} \mathbf{M}_k^T \mathbf{P}_k^{-1})^T + \mathbf{K}_{k,s} \mathbf{R}_s \mathbf{K}_{k,s}^T \quad (15)$$

469 The covariance update is a modified version of the Joseph formula adapted  
470 to the original Larsen method. This is done to ensure that the covariance  
471 matrix remains positive semi-definite. As seen in Eq. 11 and Eq. 12, the

472 extrapolation method always requires only two matrix multiplications at each  
473 time instant and the storage of two variables any time an image is acquired.

#### 474 **4. Navigation Training and Test**

475 In order to assess and validate the performances of the proposed architec-  
476 ture a testing pipeline has been put in place, exploiting the following blocks.

477 *High-fidelity dynamics Simulator.* This block takes as input a nominal guid-  
478 ance profile, like the one described in Section 2.1, and simulates the overall  
479 maneuver from lander trajectory to the sensors readings in a high-fidelity  
480 scenario. The output consists in the ground-truth trajectory and in simu-  
481 lated measurement histories for attitude and additional navigation sensors  
482 (i.e. altimeters) necessary for algorithm validation. Since the whole ma-  
483 neuver takes place in close proximity to the lunar ground, only the Moon  
484 gravitational pull is included in the translational dynamics. The LP165P  
485 spherical harmonics model up to the 165<sup>th</sup> order [44] is adopted. Distur-  
486 bances in both direction and magnitude of thrust are included. The nominal  
487 thrust vector is rotated by a random angle with normal distribution with  
488 zero mean and standard deviation  $\sigma = 1^\circ$ . Thrust magnitude is perturbed  
489 by a Gaussian noise with standard deviation 23 N (1 % of the assumed throt-  
490 tleable thrust). The proposed navigation system provides an estimate of the  
491 translation states only, but relies on attitude determination to identify the  
492 camera pointing direction: then, attitude estimation errors could have an  
493 impact on navigation performances. The spacecraft rotational dynamics are  
494 not simulated: the navigation camera is assumed to maintain a nominal nadir  
495 pointing, while a Gaussian noise with standard deviation  $\sigma = 1^\circ$  is added on

496 the three Euler Angles to represent attitude determination errors. A zero  
497 mean Gaussian white noise is added to the ground-truth altitude to simu-  
498 late altimeter measures. A standard deviation of 1% of the current altitude  
499 is assumed, reflecting the actual behavior of the laser altimeter technology.  
500 The whole model is implemented in a *Matlab-Simulink* environment, with al-  
501 titude measurements generated at frequency 8 Hz. An example of simulated  
502 altitude measurement is reported in Fig. 11, compliant with the scenario  
503 described in Section 2.

504 *Navigation images rendering.* As reported in section 3.1, a 3D rendering  
505 tool is adopted to simulate realistic images as generated by the on-board  
506 navigation camera. *Pangu* is exploited for such purpose, taking as input  
507 the ground-truth generated by the simulator block for both trajectory and  
508 spacecraft attitude and outputting a sequence of images sampled at 1 Hz.

509 *AI-IP block.* This block includes the application of the trained crater detector  
510 to the generated images to extract the centers and the radii of the detected  
511 craters, expressed in pixels coordinates in the camera frame. This procedure  
512 is executed in a *Python* environment.

513 *Navigation algorithm simulator.* The final block is instead in charge of run-  
514 ning the crater matching and the filtering tasks in a step-wise fashion, ex-  
515 ploiting as inputs all the generated measurements, i.e. the ODN products  
516 and the altimeter readings, dealing also with the two different sampling rates.  
517 Each second of simulation, the algorithm given its current best state estimate,  
518 runs the crater matching procedure, comparing the detected craters to the  
519 pruned craters database and pass to the filter the measurements of all the

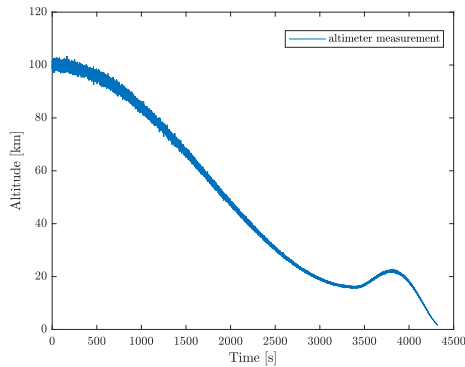


Figure 11: Simulated measured altitude.

520 matches retrieved. The state estimate is then be compared to the ground-  
 521 truth trajectory and, together with the estimated covariance matrix, used to  
 522 assess the overall strategy performances. Also this block is implemented in  
 523 a *Matlab-Simulink* environment.

#### 524 4.1. CNN training

525 The use of a pre-trained MobileNetV2 model allowed to rely on transfer  
 526 learning to speed-up the training process, achieving at the same time good  
 527 results even with a relatively small training set like the one described in  
 528 Section 3.1. A fine-tuning of the original weights of the last two network  
 529 branches was sufficient for converging to an optimal solution, while all the  
 530 other weights were maintained fixed at the original value. No data augmenta-  
 531 tion was applied or required. The adopted loss function replicates the original  
 532 implementation by Liu et al. [36], and it is composed by two contributions  
 533 to be minimized concurrently:

$$L(x, c, l, g) = \frac{1}{N} (L_{\text{conf}}(x, c) + \alpha L_{\text{loc}}(x, l, g)) \quad (16)$$

534 where  $L_{\text{loc}}$  is a localization loss that reduces the L1 distance between the  
 535 predicted box  $l$  and the ground-truth box  $g$ , and  $L_{\text{conf}}$  is a confidence loss  
 536 that expresses the confidence level for a particular image crop to pertain to a  
 537 particular class  $c$ . The  $x$  variable is an indicator for matching the  $i$ th default  
 538 box for the  $j$ th ground-truth box of category  $p$ .

539 The network is trained on the dataset presented in Section 3.1, with batch  
 540 size optimized to 16 samples, and learning rate optimized to 0.001, using the  
 541 Adam optimizer [45]. The train-validation split equals to 80-20%. Test  
 542 images are those generated for the trajectories: sequential images coming  
 543 from the same Pangu rendered Moon region. Transfer learning considerably  
 544 speeds-up the training process, avoiding the burden to learn low-level fea-  
 545 tures, inherited from the pre-trained network. Actual learning, enabled for  
 546 higher layers only, tailors the network over the specific problem even with a  
 547 relatively small dataset: the loss function reached its minimum in 150 epochs.  
 Relevant statistical metrics on the test dataset are reported in Tab. 2.

Table 2: ODN statistical performance metrics on the test dataset.

<b>Metric</b>	<b>Value</b>
Precision	0.6
Recall	0.9
F1-score	0.7
Mean IoU	0.7

548



549 *4.2. Craters detection and matching performance*

550 In this section, the assessment of the network capabilities in detecting  
551 craters, and of their subsequent matching within the crater database is pre-  
552 sented. Fig. 12 shows the results of the crater matching task for a sample  
553 image never seen by the network during the training phase. Craters detected  
554 by the ODN (red) are matched to the ground truth database (yellow/green).  
555 On the test set, the average correct match percentage is nearly  $\sim 75\%$  in  
556 each frame. Craters detection delivers an average localization error of  $\sim 3$  px  
557 in the LoS, as reported in Fig. 14, in which the average center location error  
558 for each frame associated with the relative standard deviation of the error  
559 distribution is shown. Please note that such error is only related with the  
560 ODN crater detection on each frame.

561 The radius fit output by the network is generally larger than the ground-  
562 truth, as shown in Fig. 13 for an example image. A possible motivation lies  
563 in the ODN post-processing stage, in which the crater radius is computed by  
564 assuming the bounding box inscribed into a circular shape. Nevertheless, this  
565 issue does not affect the absolute navigation itself, but rather the matching  
566 process with the database given that the KD-tree search is performed in  
567 the three dimensions  $[x, y, \rho]$ . Figure 15 shows the histogram of the radius  
568 estimation error: the average error is  $\sim 15\%$  with respect to the ground-truth.

569 The number of detected craters is deemed as sufficient for the required  
570 accuracy; indeed, it is in the order of  $\sim 50$  detected craters for each frame.  
571 Figures 16 and 17 show the frequency of the number of detected craters in  
572 the prototyping trajectory.

573 An inference time on the network of 0.02 s per image on a Nvidia RTX

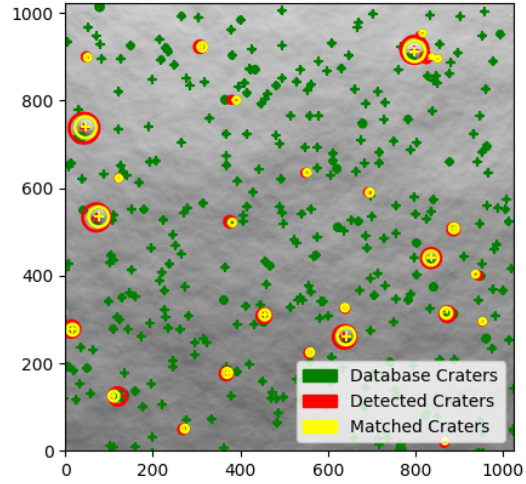


Figure 12: Example of crater detection and matching. The green craters are those extracted from the database. Given the limited size, they are discarded from the matching procedure.

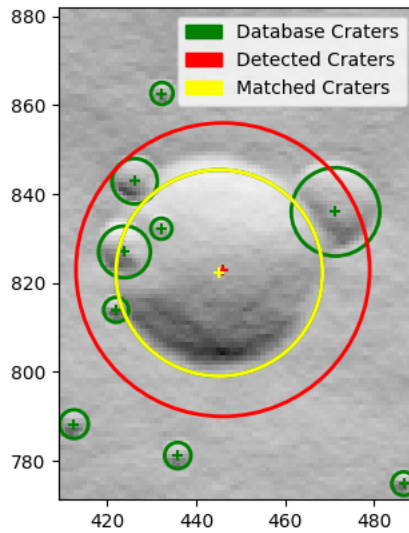


Figure 13: Wrong estimation of crater diameter. The detected diameter is larger than the database ones, due to the ODN post-processing.

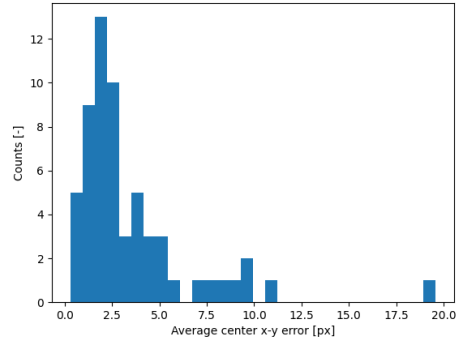


Figure 14: LoS detection errors in pixel between database and detected craters.

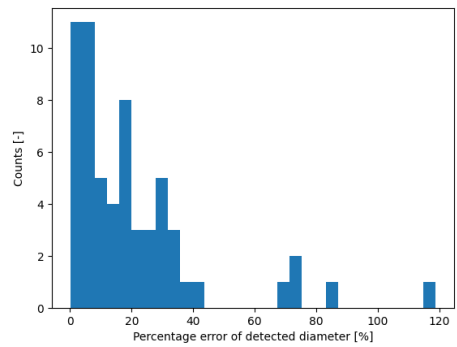


Figure 15: Diameter estimation error in detected craters.

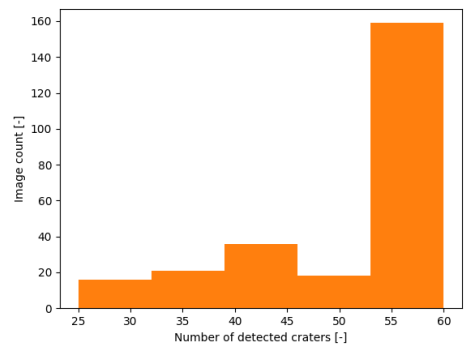


Figure 16: Detected craters distribution along a portion of the prototyping trajectory.

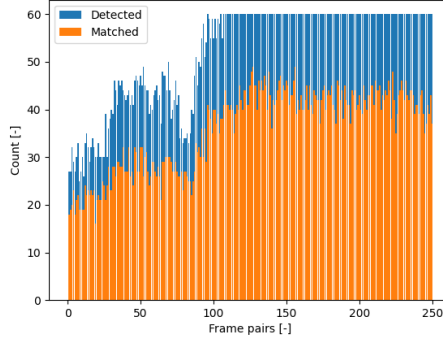


Figure 17: Detected and matched craters distribution along a portion of the prototyping trajectory.

574 Titan X GPU (or 57 frame per seconds, with FP32 model precision) was  
 575 preliminary assessed. No model optimization has been performed for the  
 576 test execution. In order to obtain a better estimation of the potential per-  
 577 formance in flight, the network has been implemented also on a Raspberry  
 578 Pi 4 equipped with an Intel Movidius Neural Compute Stick. This system  
 579 is built around the Intel Myriad 2 VPU, a possible future architecture for  
 580 AI systems in space applications, that has already proven effective in flight  
 581 [12, 13]. On Myriad hardware, with no code optimization, the inference time  
 582 increases to 0.4 s per image (or 2.5 frames per seconds), a value compatible  
 583 with the needs of autonomous navigation.

#### 584 *4.3. Navigation Prototyping: numerical results*

585 The full pipeline coupling AI-IP and NAV module has been tested using a  
 586 sample trajectory, resembling the scenario described in section 2. The craters  
 587 database (cfr. [46]) linked to the absolute navigation is used down to an  
 588 altitude of roughly  $\sim 20$  km. Below such altitude, the database spatial density

589 becomes lower than the captured FOV on the surface resulting in very few  
590 craters to be matched. The issue can be easily solved by refining the database  
591 list or coupling the absolute navigation with a relative navigation module that  
592 performs frame-to-frame motion estimation. The tuning parameters used for  
593 the simulations are reported in Tab. 3.

594 Figure 18 reports an instant in time, showing the different navigation  
595 modules performing the task. The database filtering restrains the search  
596 region in longitude and latitude coordinates, then the detected craters are  
597 matched using location and diameter as descriptors. Please note that the  
598 number of detected and processed craters is limited by the maximum craters  
599 variable in Tab. 3, which aims at keeping the number of processed craters  
600 within an acceptable range for navigation performance without overburden-  
601 ing the computational cost for subsequent real hardware implementation.  
602 The navigation estimate is reported in Fig. 19. The horizontal and vertical  
603 error are reported instead of the three-axis results. The vertical error is the  
604 projection of the error  $\Delta = \mathbf{R}_{nav} - \mathbf{R}_{gt}$  along the radial direction. The norm  
605 of the along-track and across-track error is combined in the horizontal one.  
606 The navigation yields an estimation error  $\sim 200$  m along the trajectory, both  
607 for vertical and horizontal error, which is aligned with the expected perfor-  
608 mance at these relevant altitudes. The small peak present in the plot refers  
609 to the passage on the North Pole. Such degradation is due to the fact that,  
610 in that area, the database filtering is performed on a spherical cap rather  
611 than a margined projected FOV. This is done at high latitude (i.e. above  
612  $88^\circ$ ) in order to avoid any singularities or wrapping errors at the polar point.

Parameter	Value	Description
MAX_N_CRAT	50	Maximum number of processed craters
$P_0$	$\text{diag}(10^4 \mathbf{I}_{3 \times 3}, 10^0 \mathbf{I}_{3 \times 3})$	Initial Covariance Matrix
$R_{elem}$	$10^4 \mathbf{I}_{2 \times 2}$	Elementary crater localization error covariance
$R_{alt}$	$10^2$	Elementary altimeter error variance

Table 3: Simulation parameters

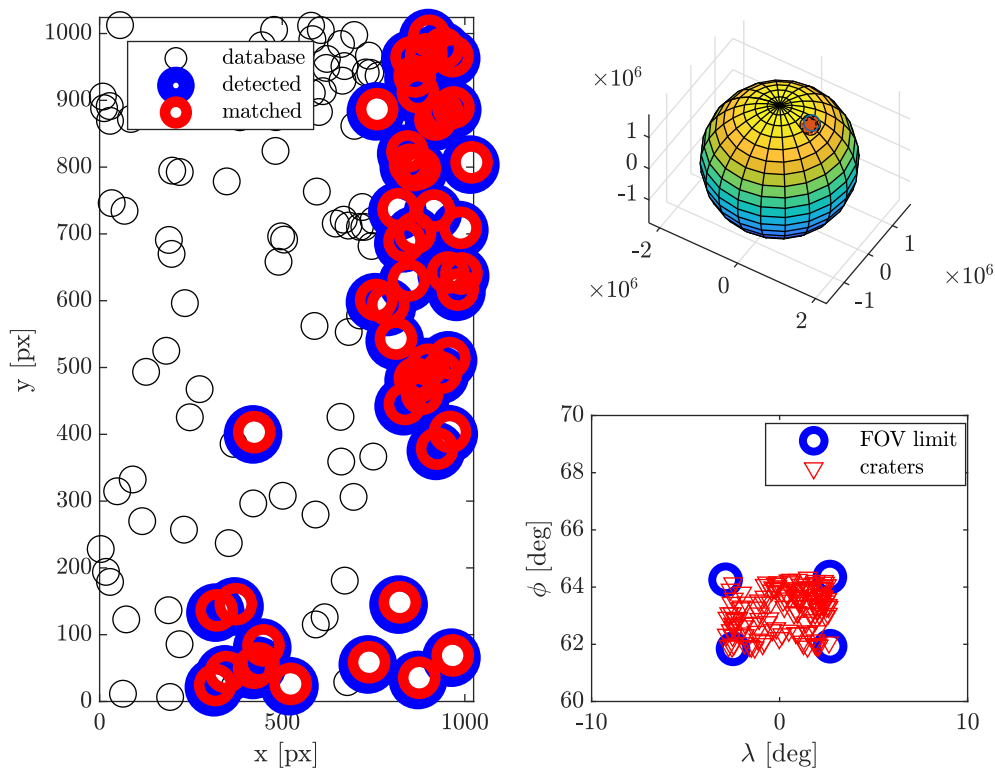


Figure 18: Running navigation performing  $\lambda$ - $\phi$  database searching and matching. The database filtering restrains the search region in longitude and latitude coordinates (bottom right), then the detected craters are matched using location and diameter as descriptors (top left).

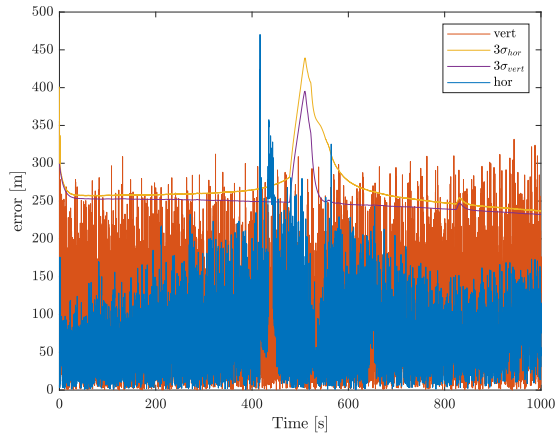


Figure 19: Estimation horizontal and vertical error for absolute navigation.

613 **5. Conclusion**

614 The paper proposed an AI-based Optical Navigation algorithm to per-  
 615 form absolute navigation during Lunar landing. A successful integration of  
 616 both the detection ODN and the matching and estimation algorithm has been  
 617 presented. The ODN network can successfully retrieve the Moon craters in  
 618 an image. The crater detection delivers excellent center localization results  
 619 (below  $\sim 3$  px) with respect to database ones, on average. This result pro-  
 620 vides the required performance for the subsequent matching task. The crater  
 621 diameters are slightly over-estimated due to ODN post-processing, neverthe-  
 622 less the prototyping tests did not show any criticalities for such behavior.  
 623 However, for future development, an additional consolidation may include a  
 624 RANSAC-like algorithm to filter out the outliers matching.

625 The database crater matching for absolute navigation has been devel-  
 626 oped and tested: results showed that each detected crater was matched to  
 627 database ones, with a small percentage of false matches. The whole pipeline

628 for absolute navigation, including AI-IP e NAV filter, has been implemented  
629 and tested in a sample trajectory at prototype level, taking into account the  
630 injection of delayed measurements. The sample scenario demonstrated that  
631 the navigation system can meet the performance requirements. Moreover,  
632 the complete pipeline for dataset generation has been set-up and used to  
633 create the prototyping dataset.

634 The presented work foresees implementation on real hardware with del-  
635 icate execution time constraints, hence it is critical to reduce the computa-  
636 tional burden on-board. The main objective is to assess the applicability of  
637 CNN-based crater detector to the absolute navigation task. In particular, the  
638 usage of such ODN architecture, compared with classical algorithms, may be  
639 beneficial under several aspects: first of all, the amount of crater detections  
640 that ODN-detector produces is robust to disturbances or modifications of  
641 the image quality due to Gaussian noise, shot noise, brightness levels, as well  
642 as different illumination conditions. This robustness to visual alterations  
643 supports the feasibility of CNN-based techniques as reliable navigation ar-  
644 chitectures that do not imply a high level of human input or tuning. This is  
645 confirmed also by other works [21, 22, 47, 16]. Moreover, as mentioned, this  
646 work is aimed at the subsequent integration in real flight-like hardware: the  
647 achieved inference time makes the ODN a promising, and fast, alternative to  
648 the iterative, and slower, processes of template matching and thresholding  
649 required in classical techniques [10]. In this way, and end-to-end navigation  
650 cycle, including the image processing, can be achieved at 1 Hz frequency.



651 **Acknowledgments**

652 The presented work was funded by the European Space Agency, under  
653 the ESA Contract No. 4000129466/19/NL/CRS. The authors would like to  
654 acknowledge the support from the AIVIONIC consortium: DEIMOS Engen-  
655 haria S.A. (Portugal) as prime contractor; AIKO SRL (Italy), Politecnico di  
656 Milano (Italy), Fortiss GmbH (Germany), Ubotica (Ireland) and DEIMOS  
657 Space S.L.U. (Spain).

658 **References**

- 659 [1] A. Colagrossi, M. Lavagna, Dynamical analysis of rendezvous and dock-  
660 ing with very large space infrastructures in non-Keplerian orbits, *CEAS*  
661 *Space Journal* 10 (1) (2018) 87–99. doi:10.1007/s12567-017-0174-4.
- 662 [2] A. Colagrossi, V. Pesce, L. Bucci, F. Colombi, M. Lavagna, Guidance,  
663 navigation and control for 6DOF rendezvous in Cislunar multi-body  
664 environment, *Aerospace Science and Technology* 114 (2021) 106751.  
665 doi:10.1016/j.ast.2021.106751.
- 666 [3] F. Colombi, A. Colagrossi, M. Lavagna, Characterisation of 6DOF natu-  
667 ral and controlled relative dynamics in cislunar space, *Acta Astronautica*  
668 (2021). doi:10.1016/j.actaastro.2021.01.017.
- 669 [4] S. Li, P. Cui, H. Cui, Vision-aided inertial navigation for pinpoint plan-  
670 etary landing, *Aerospace Science and Technology* 11 (6) (2007) 499–506.  
671 doi:https://doi.org/10.1016/j.ast.2007.04.006.

- 672 [5] V. Pesce, S. Silvestrini, M. Lavagna, Radial basis function neural  
673 network aided adaptive extended Kalman filter for spacecraft rela-  
674 tive navigation, *Aerospace Science and Technology* 96 (2020) 105527.  
675 doi:10.1016/j.ast.2019.105527.
- 676 [6] A. Pasquale, S. Silvestrini, A. Capannolo, P. Lunghi, M. Lavagna, Small  
677 bodies non-uniform gravity field on-board learning through Hopfield  
678 Neural Networks, *Planetary and Space Science* 212 (December 2021)  
679 (2022) 105425. doi:10.1016/j.pss.2022.105425.
- 680 [7] S. Silvestrini, M. Lavagna, Neural-aided GNC reconfiguration algorithm  
681 for distributed space system: development and PIL test, *Advances in*  
682 *Space Research* 67 (5) (2021) 1490–1505. doi:10.1016/j.asr.2020.12.014.
- 683 [8] S. Silvestrini, M. Lavagna, Neural-based predictive control for safe au-  
684 tonomous spacecraft relative maneuvers, *Journal of Guidance, Control*  
685 *and Dynamics* (2021). doi:10.2514/1.G005481.
- 686 [9] S. Silvestrini, M. Lavagna, Relative Trajectories Identification in Dis-  
687 tributed Spacecraft Formation Collision-Free Maneuvers using Neural-  
688 Reconstructed Dynamics, in: *AIAA Scitech 2020 Forum*, no. January,  
689 2020, pp. 1–14. doi:10.2514/6.2020-1918.
- 690 [10] L. Singh, S. Lim, On lunar on-orbit vision-based navigation: Ter-  
691 rain mapping, feature tracking driven EKF, *AIAA Guidance, Nav-*  
692 *igation and Control Conference and Exhibit* (August) (2008) 1–18.  
693 doi:10.2514/6.2008-6834.

- 694 [11] C. Xu, X. Huang, M. Li, D. Wang, Landmark database selec-  
695 tion for vision-aided inertial navigation in planetary landing  
696 missions, *Aerospace Science and Technology* 118 (2021) 107040.  
697 doi:<https://doi.org/10.1016/j.ast.2021.107040>.  
698 URL [https://www.sciencedirect.com/science/article/pii/  
699 S1270963821005502](https://www.sciencedirect.com/science/article/pii/S1270963821005502)
- 700 [12] G. Giuffrida, L. Diana, F. de Gioia, G. Benelli, G. Meoni, M. Do-  
701 nati, L. Fanucci, Cloudscout: A deep neural network for on-board  
702 cloud detection on hyperspectral images, *Remote Sensing* 12 (14) (2020).  
703 doi:10.3390/rs12142205.
- 704 [13] G. Mateo-Garcia, J. Veitch-Michaelis, L. Smith, S. V. Oprea, G. Schu-  
705 mann, Y. Gal, A. G. Baydin, D. Backes, Towards global flood mapping  
706 onboard low cost satellites with machine learning, *Scientific Reports* 11  
707 (2021) 7249. doi:10.1038/s41598-021-86650-z.
- 708 [14] F. Baldini, A. Anandkumar, R. M. Murray, Learning pose estimation  
709 for uav autonomous navigation and landing using visual-inertial sensor  
710 data, in: *2020 American Control Conference (ACC)*, 2020, pp. 2961–  
711 2966. doi:10.23919/ACC45564.2020.9147400.
- 712 [15] R. Furfaro, I. Bloise, M. Orlandelli, P. Di Lizia, F. Topputo, R. Linares,  
713 Deep learning for autonomous lunar landing, in: *2018 AAS/AIAA As-  
714 trodynamics Specialist Conference, Snowbird, UT, 2018*.
- 715 [16] S. Wang, R. Clark, H. Wen, N. Trigoni, Deepvo: Towards end-to-  
716 end visual odometry with deep recurrent convolutional neural networks,

- 717 in: 2017 IEEE International Conference on Robotics and Automation  
718 (ICRA), 2017, pp. 2043–2050. doi:10.1109/ICRA.2017.7989236.
- 719 [17] E. Brachmann, C. Rother, Learning less is more - 6d camera local-  
720 ization via 3d surface regression, in: 2018 IEEE/CVF Conference  
721 on Computer Vision and Pattern Recognition, 2018, pp. 4654–4662.  
722 doi:10.1109/CVPR.2018.00489.
- 723 [18] E. Emami, T. Ahmad, G. Bebis, A. Nefian, T. Fong, Lunar crater de-  
724 tection via region-based convolutional neural networks, in: 49th Lunar  
725 and Planetary Science Conference, The Woodlands, TX, 2018.
- 726 [19] E. Emami, T. Ahmad, G. Bebis, A. Nefian, T. Fong, Crater detection  
727 using unsupervised algorithms and convolutional neural networks, IEEE  
728 Transactions on Geoscience and Remote Sensing 57 (8) (2019) 5373–  
729 5383. doi:10.1109/TGRS.2019.2899122.
- 730 [20] A. Silburt, M. Ali-Dib, C. Zhu, A. Jackson, D. Valencia, Y. Kissin,  
731 D. Tamayo, K. Menou, Lunar crater identification via deep learning,  
732 Icarus 317 (2019) 27–38. doi:10.1016/j.icarus.2018.06.022.
- 733 [21] L. Downes, T. J. Steiner, J. P. How, Deep Learning Crater Detection  
734 for Lunar Terrain Relative Navigation, in: AIAA Scitech 2020 Forum,  
735 2020, pp. 1–12. doi:10.2514/6.2020-1838.
- 736 [22] L. M. Downes, T. J. Steiner, J. P. How, Lunar terrain relative navi-  
737 gation using a convolutional neural network for visual crater detection,  
738 in: 2020 American Control Conference (ACC), 2020, pp. 4448–4453.  
739 doi:10.23919/ACC45564.2020.9147595.

- 740 [23] W. Park, Y. Jung, H. Bang, J. Ahn, Robust crater triangle matching al-  
741 gorithm for planetary landing navigation, *Journal of Guidance, Control,*  
742 *and Dynamics* 42 (2) (2019) 402–410. doi:10.2514/1.G003400.
- 743 [24] J. qing Chen, P. yuan Cui, H. tao Cui, Automated detection and classifi-  
744 cation for craters based on geometric matching, in: J. C. Zarnecki, C. A.  
745 Nardell, R. Shu, J. Yang, Y. Zhang (Eds.), *International Symposium on*  
746 *Photoelectronic Detection and Imaging 2011: Space Exploration Tech-*  
747 *nologies and Applications*, Vol. 8196, International Society for Optics  
748 and Photonics, SPIE, 2011, pp. 543 – 548. doi:10.1117/12.901020.
- 749 [25] W. Shao, J. Xie, L. Cao, J. Leng, B. Wang, Crater matching algorithm  
750 based on feature descriptor, *Advances in Space Research* 65 (1) (2020)  
751 616–629. doi:10.1016/j.asr.2019.09.031.
- 752 [26] R. Opromolla, G. Fasano, Visual-based obstacle detec-  
753 tion and tracking, and conflict detection for small UAS  
754 sense and avoid, *Aerospace Science and Technology* (2021)  
755 107167doi:https://doi.org/10.1016/j.ast.2021.107167.
- 756 [27] NASA’s lunar exploration program overview, retrieved August 7, 2021  
757 (2020).  
758 URL [https://www.nasa.gov/sites/default/files/atoms/files/](https://www.nasa.gov/sites/default/files/atoms/files/artemis\_plan-20200921.pdf)  
759 [artemis\\\_plan-20200921.pdf](https://www.nasa.gov/sites/default/files/atoms/files/artemis\_plan-20200921.pdf)
- 760 [28] P. Tripathi, R. Garg, Spectral characterization of shoemaker crater at  
761 the lunar south pole: possible science objective for the artemis iii human

- 762 mission to moon, in: ACRS 2020 - 41st Asian Conference on Remote  
763 Sensing, 2020.
- 764 [29] H. Guo, W. Fu, G. Liu, Frontiers of moon-based earth observation,  
765 in: Scientific Satellite and Moon-Based Earth Observation for Global  
766 Change, Springer, 2019, pp. 541–590.
- 767 [30] P. Lunghi, R. Armellin, P. Di Lizia, M. Lavagna, et al., Semi-analytical  
768 adaptive guidance computation based on differential algebra for au-  
769 tonomous planetary landing, in: 26th AAS/AIAA Space Flight Me-  
770 chanics Meeting, Vol. 158, Univelt, 2016, pp. 2003–2022.
- 771 [31] P. Lunghi, M. Lavagna, R. Armellin, A semi-analytical guidance al-  
772 gorithm for autonomous landing, *Advances in Space Research* 55 (11)  
773 (2015) 2719–2738. doi:10.1016/j.asr.2015.02.022.
- 774 [32] I. Martin, M. Dunstan, M. Sanchez Gestido, Planetary surface image  
775 generation for testing future space missions with pangu, in: 2nd RPI  
776 Space Imaging Workshop, Sensing, Estimation, and Automation Labo-  
777 ratory, United States, 2019.
- 778 [33] G. Neukum, B. König, J. Arkani-Hamed, A study of lunar im-  
779 pact crater size-distributions, *The Moon* 12 (2) (1975) 201–229.  
780 doi:10.1007/BF00577878.
- 781 [34] E. Shelhamer, J. Long, T. Darrell, Fully convolutional net-  
782 works for semantic segmentation, *IEEE Transactions on Pat-  
783 tern Analysis and Machine Intelligence* 39 (4) (2017) 640–651.  
784 doi:10.1109/TPAMI.2016.2572683.

- 785 [35] O. Ronneberger, P. Fischer, T. Brox, U-net: Convolutional networks  
786 for biomedical image segmentation, in: N. Navab, J. Hornegger, W. M.  
787 Wells, A. F. Frangi (Eds.), Medical Image Computing and Computer-  
788 Assisted Intervention – MICCAI 2015, Springer International Publish-  
789 ing, Cham, 2015, pp. 234–241.
- 790 [36] W. Liu, D. Anguelov, D. Erhan, C. Szegedy, S. Reed, C.-Y. Fu, A. C.  
791 Berg, SSD: Single Shot MultiBox Detector, in: B. Leibe, J. Matas,  
792 N. Sebe, M. Welling (Eds.), Computer Vision – ECCV 2016, Springer  
793 International Publishing, Cham, 2016, pp. 21–37.
- 794 [37] M. Sandler, A. Howard, M. Zhu, A. Zhmoginov, L.-C. Chen, Mo-  
795 bileNetV2: Inverted residuals and linear bottlenecks, in: 2018  
796 IEEE/CVF Conference on Computer Vision and Pattern Recognition,  
797 2018, pp. 4510–4520. doi:10.1109/CVPR.2018.00474.
- 798 [38] T.-Y. Lin, M. Maire, S. Belongie, L. Bourdev, R. Girshick, J. Hays,  
799 P. Perona, D. Ramanan, C. L. Zitnick, P. Dollár, Microsoft COCO:  
800 Common Objects in Context, arXiv [Preprint] arXiv:1405.0312 (2015).
- 801 [39] F. Chollet, Xception: Deep learning with depthwise separa-  
802 ble convolutions, in: 2017 IEEE Conference on Computer Vi-  
803 sion and Pattern Recognition (CVPR), 2017, pp. 1800–1807.  
804 doi:10.1109/CVPR.2017.195.
- 805 [40] Lunar reconnaissance orbiter camera (lroc) database, [http://lroc.](http://lroc.sese.asu.edu/)  
806 [sese.asu.edu/](http://lroc.sese.asu.edu/), accessed: 19-02-2022.

- 807 [41] A. Comellini, D. Casu, E. Zenou, V. Dubanchet, C. Espinosa, Incorporating delayed and multirate measurements in navigation filter for  
808 autonomous space rendezvous, *Journal of Guidance, Control, and Dy-*  
809 *namics* 43 (6) (2020) 1164–1172. doi:10.2514/1.G005034.
- 811 [42] H. L. Alexander, State estimation for distributed systems with sensing  
812 delay, *SPIE Data Structures and Target Classification* 1470 (1991) 103–  
813 111.
- 814 [43] T. D. Larsen, N. A. Andersen, O. Ravn, N. K. Poulsen, Incorporation of  
815 time delayed measurements in a discrete-time Kalman filter, *Proceedings*  
816 *of the IEEE Conference on Decision and Control* 4 (December) (1998)  
817 3972–3977. doi:10.1109/cdc.1998.761918.
- 818 [44] A. Konopliv, A. Kucinskas, W. Sjogren, J. Williams, A. Binder, L. Hood,  
819 The gravity field of the moon from the lunar prospector mission (1998).
- 820 [45] D. P. Kingma, J. Ba, Adam: A method for stochastic optimization, in:  
821 3rd International Conference for Learning Representations, San Diego,  
822 CA, 2015. arXiv:1412.6980.
- 823 [46] S. J. Robbins, A New Global Database of Lunar Impact Craters >  
824 1–2 km: 1. Crater Locations and Sizes, Comparisons With Published  
825 Databases, and Global Analysis, *Journal of Geophysical Research: Plan-*  
826 *ets* 124 (4) (2019) 871–892. doi:10.1029/2018JE005592.
- 827 [47] L. M. Downes, T. J. Steiner, J. P. How, Lunar Terrain Rel-  
828 ative Navigation Using a Convolutional Neural Network for



829 Visual Crater Detection (2020) 4448–4453arXiv:2007.07702,  
830 doi:10.23919/acc45564.2020.9147595.